

Guided Disentanglement in Generative Networks

Fabio Pizzati^{1,2} · Pietro Cerri² · Raoul de Charette¹

Received: date / Accepted: date

Abstract Image-to-image translation (i2i) networks suffer from entanglement effects in presence of physics-related phenomena in target domain (such as occlusions, fog, etc), thus lowering the translation quality and variability. In this paper, we present a comprehensive method for disentangling physics-based traits in the translation, guiding the learning process with neural or physical models. For the latter, we integrate adversarial estimation and genetic algorithms to correctly achieve disentanglement. The results show our approach dramatically increase performances in many challenging scenarios for image translation.

Keywords Adversarial learning · image to image translation · feature disentanglement · adverse weather · vision and rain · GAN

1 Introduction

Image-to-image (i2i) translation GANs can learn source \mapsto target mappings in an unsupervised manner, finding great applicability in artistic style transfer, content generation, and other scenarios [96, 45, 31]. When coupled with domain adaptation strategies [28, 39, 79], they also provide an alternative to manual annotation work for synthetic to real [11] or challenging conditions generation [64, 75, 62].

Nowadays, i2i networks exhibit great performances in learning numerous characteristics of target scenes simultaneously, which would otherwise be impractical to model with alternative approaches. However, a common pitfall is their inability to accurately learn the underlying physics of the transformation [87], often generating artifacts based on inaccurate mapping of source and target characteristics, which significantly impact results. This is the case for example

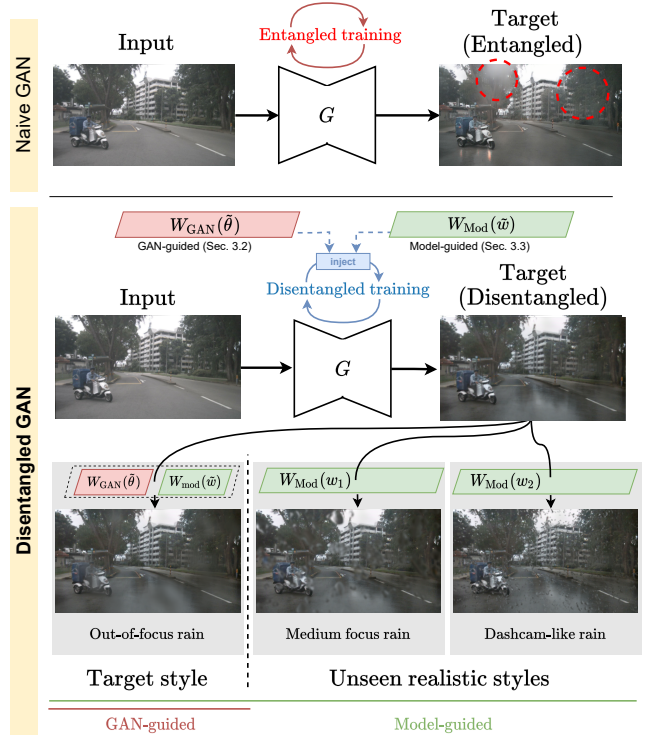


Fig. 1: **Guided disentanglement.** Our method enables disentanglement of target scenes characteristics, from $W(\cdot)$ guidance which might be neural or physical models, both differentiable and non-differentiable. While naive GANs generate *entangled target* images, we learn a *disentangled* version of the scene from guidance of model $W(\cdot)$ with estimated physical (\tilde{w}) or neural ($\tilde{\theta}$) parameters. Notice here the unrealistic raindrops entanglement in naive GANs. In contrast, our disentangled GAN prevents entanglement enabling the generation of target style ($\tilde{w}, \tilde{\theta}$) or unseen scenarios (here, w_1, w_2).

¹ Inria, 2 Rue Simone IFF, 75012 Paris, France

² Vislab, Parco Area delle Scienze 49, 43124 Parma, Italy

when learning $\text{clear} \mapsto \text{rain}$ as naive GAN translation will inevitably entangle inaccurate raindrops, as highlighted in Fig. 1 top. In this paper we show that this is amenable to the extraction of entangled representations of scene elements and physical traits. On the other hand, model-based approaches are commonly used to render well-studied elements of target domain with great realism [68, 2, 24, 80], but leaving any other domain gap unmodified.

We propose a learning-based comprehensive framework to unify generative networks with priors guidance. Our proposal relies on a disentanglement strategy integrating GAN or physics model guidance with an adversarial training having optimal parameters regressed on the target set. Ultimately, we partially render the target scene with a neural or physical model, while learning the un-modeled target characteristics with an i2i network, in a complementary manner, and we compose them as shown in Fig. 1 to get the final inference. Besides increasing image realism, our physical model-guided framework enables fine-grained control of physical parameters in rendered scenes, for increasing generated images variability regardless of the training dataset. This is obviously beneficial for outdoor robotics applications, which require resistance to various unobserved scenarios.

In this paper, we significantly extend our prior work [60], which focused on occlusion disentanglement of differentiable models, by opening to non-differentiable models (Sec. 3.3.2), with an entirely novel GAN-guided disentanglement pipeline with new ad-hoc experiments (Secs. 3.2, 4.3), a new geometry-dependent task (Sec. 4.2.2), by further extending the evaluation (Sec. 4.2.3), and finally by both extending ablations (Sec. 4.4) and discussion (Sec. 5).

2 Related works

2.1 Image-to-image translation

The seminal work on image-to-image translation (i2i) using conditional GANs on paired images was conducted by Isola et al. [31], while [82] exploits multi-scale architectures to generate HD results. Zhu et al. [96] propose a framework working with unpaired images introducing cycle consistency, exploited also in early work on paired multimodal image translation [97]. A similar idea is proposed in [90].

There has been a recent trend for alternatives to cycle consistency for appearance preservation in several approaches [3, 8, 18], to increase focus on global image appearance and reduce it on unneeded textural preservation. In [57], they propose a cycle consistency free multi-modal framework. Many methods also include additional priors to increase translation consistency, using objects [75, 10], instance [54], geometry [85, 6] or semantics [37, 65, 78, 13, 99, 98, 40, 50, 49]. Other approaches learn a shared latent space using a Variational Autoencoder, as in Liu et al. [45].

Recently, attention-based methods were proposed, to modify partly input images while keeping domain-invariant regions unaltered [53, 51, 77, 34, 42]. Alternatively, spatial attention was exploited to drive better the adversarial training on unrealistic regions [43]. Some methods focus instead on generating intermediate representations of source and target [22, 44] or continuous translations [61, 48]. In the recent [20], authors exploit similarity with retrieved images to increase translation quality.

2.2 Disentanglement in i2i

Disentangled representations of content and appearance seem to be an emerging trend to increase i2i outputs quality. Recently, Park et al. [58] proposed a contrastive learning based framework to disentangle content from appearance based on patches. MUNIT [29], DRIT [36] and TSIT [33] exploit disentanglement between content and style to achieve one-to-many translations. The idea is further extended in FUNIT [46] to achieve few-shot learning. In COCO-FUNIT [71], style extraction is conditioned on the image content to preserve fine-grained consistency. In HiDT [4], they exploit multi-scale style injection to reach translations of high definition, while [86, 41] conditions disentanglement on domain supervision. Following different reasoning, [35] disentangles representations enforcing orthogonality. In [32], they prevent semantic entanglement by using gradient regularization.

Multi-domain i2i methods [14, 66, 5, 88, 30, 84, 56] could be also exploited for disentangling representations among different domains, at the cost of requiring annotated datasets with separated physical characteristics – practically inapplicable for real images. Recent frameworks [93, 15] unify multi-domain and multi-target i2i exploiting multiple disentangled representations. Some works [76, 38], detach from literature proposing hierarchical generation. In [11], instead, they learn separately albedo and shading, regardless of the general scene. A similar result is performed by [47], only using unpaired images. Recently, also VAE-based alternatives have emerged [9].

Disentangled representations could also help in physics-driven i2i tasks, such as [89] where a fog model is exploited to dehaze images. Similarly, Gong et al. [21] perform fog generation exploiting paired simulated data. Even though these methods effectively learn physical transformations in a disentangled manner, they simply ignore the mapping of other domain traits.

2.3 Physics-based generation

Many works in literature rely on rendering to generate physics-based traits in images, for rain streaks [19, 24, 80,

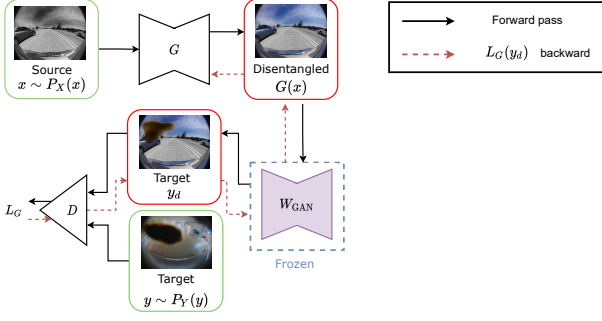


Fig. 2: **GAN-guided disentanglement.** We exploit here a separate frozen GAN (W_{GAN}) which renders specific target traits (here, dirt) on generator G output images before forwarding them to the discriminator D . This further impacts disentanglement in G .

[83, 70], snow [7], fog [72, 24] or others. In many cases, physical phenomena cause occlusion of the scene – well studied in the literature. For instance, many models for raindrops are available, exploiting surface modeling and ray tracing [68, 69, 27]. In [92], raindrop motion dynamics are also modeled. Recent works instead focus on photorealism relaxing physical accuracy constraints [63, 2]. A general model for lens occluders has been proposed in [23]. Logically, it is extremely challenging to entirely simulate the appearance of scene encompassing multiple physical phenomena (for rain: rain streaks, raindrops on the lens, reflections, etc.), hence in [80] they also combine i2i networks and physics-based rendering. However, this is quite different from our objective since they assume to physically model features not present in the target images. To the best of our knowledge, there is no method which unifies rendering based on physical models and i2i translations in a complementary manner.

3 Guided disentanglement

The motivation of our work is that standard i2i GANs solely rely on context mapping between source and target only. In some setups, however, target domain encompasses known visual traits partially occluding the scene, for example adverse weather or lens occlusions, thoroughly studied in the literature. Hence, it may be amenable to integrate *a priori* models in the adversarial learning process to boost performances.

To model i2i transformations as a composition of characteristics, we propose a disentangled setting where the i2i GAN compensates the missing (unmodeled) traits to recreate the complete target style. Disentanglement is achieved relying either on a full neural GAN-guided shown in Fig. 2 (Sec. 3.2) or physics model-guided shown in Fig. 3 (Sec. 3.3) setting. In the latter, we exploit existing physical models for disentanglement, using as only prior the nature of physical trait we aim to disentangle (e.g. raindrop,

dirt, fog, etc.). Furthermore, we estimate target parameters of the physical model (Sec. 3.3.1) to ease disentangled learning as well as to reduce differences with target. Our approach boosts image quality and realism guiding model injection during training with gradient-based guidance (Sec. 3.3.3). An extensive explanation of training strategies is in Sec. 4.

3.1 Adversarial disentanglement

In image-to-image translation we aim to learn a transformation between a source X and a target Y , thus mapping $X \mapsto Y$ in an unsupervised manner. We assume that Y appearance is partly characterized by a well-identified phenomenon such as occlusions on the lens (e.g. rain, dirt) or weather phenomena (e.g. fog). Hence, we propose a sub-domain decomposition [62] of $Y = \{Y_W, Y_T\}$, separating the identified traits (Y_W) from the other ones (Y_T). We assume this only on target, so $X = \{X_T\}$. In adversarial learning, the task of the generator is to approximate the probability distributions P_X and P_Y associated with the problem domains, such as

$$\begin{aligned} \forall x \in X, x &\sim P_X(x), \\ \forall y \in Y, y &\sim P_Y(y). \end{aligned} \quad (1)$$

For simplicity, we assume that the traits identifiable in this manner are independent from the recorded scene. For instance, physical properties of raindrops on a lens (such as thickness or position) do not change with the scene, as it happens also with fog, where visual effects are only depth-dependent. Therefore, Y_W is fairly independent from Y_T , hence we formalize P_Y as a joint probability distribution with independent marginals, such as

$$P_Y(y) = P_{Y_W, Y_T}(y_W, y_T) = P_{Y_W}(y_W)P_{Y_T}(y_T). \quad (2)$$

Intuitively, modeling one of the marginals with *a priori* knowledge will force the GAN to learn the other one in a disentangled manner. During training, this translates into injecting features belonging to Y_W before forwarding the images to the discriminator, which will provide feedback on the general realism of the image.

Formally, we modify a LSGAN [52] training, which enforces adversarial learning minimizing

$$\begin{aligned} y_d &= G(x), \\ L_{\text{gen}} &= L_G(y_d) = \mathbb{E}_{x \sim P_X(x)}[(D(y_d) - 1)^2], \\ L_{\text{disc}} &= L_D(y_d, y) = \mathbb{E}_{x \sim P_X(x)}[D(y_d)^2] + \\ &\quad + \mathbb{E}_{y \sim P_Y(y)}[(D(y) - 1)^2], \end{aligned} \quad (3)$$

where L_{gen} and L_{disc} are tasks of generator G and discriminator D , respectively. We instead learn a disentangled mapping injecting modeled traits $W(\cdot)$ on translated images. We

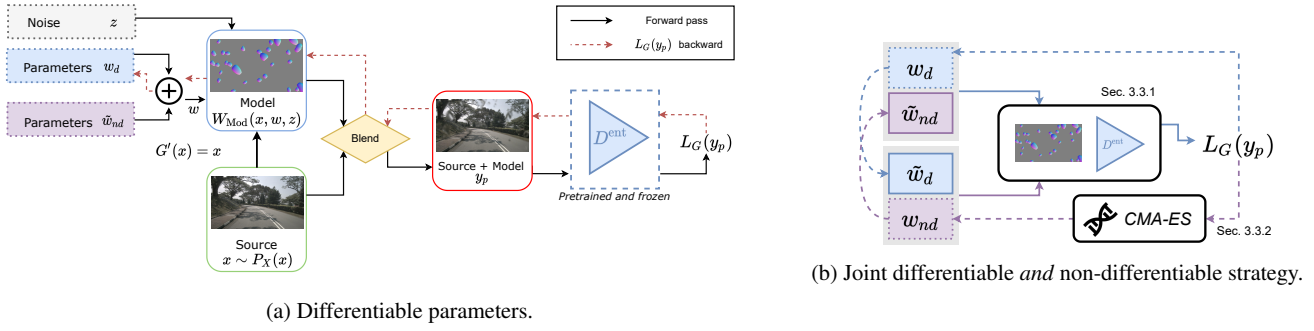


Fig. 4: **Model-guided parameters estimation.** **a)** We exploit a pretrained discriminator D^{ent} , to calculate an adversarial loss L_G on source data augmented with the model W_{Mod} having differentiable parameters w_d . In this process, the gradient flows only in direction of the differentiable parameters. **b)** We optimize until convergence differentiable (blue) and non-differentiable (purple) parameters, alternatively reaching new minima (\tilde{w}_d and \tilde{w}_{nd}) used during optimization of the other parameter set. While differentiable parameters are regressed (Sec. 3.3.1), non-differentiable ones require black-box genetic optimization (Sec. 3.3.2), here CMA-ES [26].

adversarial-based strategies to regress optimal \tilde{w} mimicking target dataset appearance. This is in fact needed for disentangled training where we assume modeled traits to resemble target ones. Other parameters are of stochastic nature (e.g. drop positions on the image) and are encoded as a noise z regulating random characteristics. Additionally, some models appearance – like refractive occlusions – vary with the underlying scene¹ s , so we write $W_{Mod}(\cdot) = W_{Mod}(s, w, z)$, with $s = G(x)$. Following our model-guided pipeline in Fig. 3, if \tilde{w} properly estimates target physical parameters, $W_{Mod}(s, \tilde{w}, z)$ estimates marginal $P_{Y_W}(y_W)$ which again enables disentanglement.

During inference instead, w and z can be arbitrarily varied, greatly increasing generation variability while still obtaining realistic target scene rendering. In the following, we describe our adversarial parameter estimation strategy, while distinguishing differentiable (w_d) and non-differentiable (w_{nd}) parameters, such that $w = \{w_d, w_{nd}\}$.

3.3.1 Adversarial differentiable parameters estimation

To estimate the target optimized derivable parameters \tilde{w}_d , we exploit an adversarial-based strategy benefiting from entanglement in naive trainings. Considering a naive baseline trained on source \mapsto target mapping, where target entangles two sub domains, the *entangled* discriminator D^{ent} successfully learns to distinguish fake target images. This results in being able to discriminate $P_X = P_{X_S}$ from $P_Y = P_{Y_T}(y_S)P_{Y_W}(y_W)$. Considering a simplified scenario where P_{Y_T} is arbitrarily confused with source domain, such that $P_{Y_T} = P_{X_T}$, regressing w_d is the only way to minimize the domain shift. In other words, considering the derivable model parametrized by w_d , the above domains

¹ In Sec. 5, we explain how W_{Mod} depending of s is not violating the independence assumption of Eq. 2, and evaluate its effect in Sec. 4.4.

confusion prevents any changes in the scene. To minimize differences between source and target the network is left with updating the injected physical model appearance, ultimately regressing w_d .

Fig. 4a shows our differentiable parameter pipeline. From a training perspective, we first pretrain an i2i baseline (e.g. MUNIT [29]), learning an entangled $X \mapsto Y$ mapping. We then freeze the entangled discriminator (D^{ent}) and use it to solve

$$y_p = \alpha_w x + (1 - \alpha_w) W_{Mod}(x, w, z), \min_{w_d} L_G(y_p), \quad (5)$$

backpropagating the GAN loss through the differentiable model. Since many models may encompass pixelwise transparency, often the blending mask α_w is $\alpha_w = \alpha_w(w, z)$. Freezing the discriminator is mandatory as we aim to preserve the previously learned target domain appearance during the estimation process. After convergence, we extract the optimal parameter set \tilde{w}_d . Alternatively, \tilde{w}_d could be manually tuned by an operator, at the cost of menial work and inaccuracy, possibly leading to errors in the disentanglement.

From Fig. 4a, notice that the gradient flows only through differentiable parameters (w_d). We now detail our strategy to optimize jointly inevitable non-differentiable parameters (w_{nd}).

3.3.2 Genetic non-differentiable parameters estimation

The previously described strategy only holds for differentiable parameters w_d , since we use backpropagation of an adversarial loss. Nonetheless, many models include non-differentiable parameters w_{nd} that could equally impact the realism of our model $W_{Mod}(\cdot)$. For example, a model generating raindrops occlusion would include differentiable parameters like the imaging focus, but also non-differentiable

ones like the shape or number of drops – all of which significantly impact visual appearance. Incorrect sizing of non-differentiable parameters w_{nd} can lead to a wrong disentanglement. Manual approximation of optimal w_{nd} parameters via trial-and-error might also be cumbersome or impractical for vast search space. To circumvent this, we exploit a genetic strategy estimating w_{nd} .

In our method, non-differentiable parameters are fed to a genetic optimization strategy. The evolutionary criteria remain the same as for differentiable parameters, that is the pretrained discriminator (D^{ent}) adversarial loss. In practice, to avoid noisy updates after genetic estimation, we average adversarial loss over a fixed number of samples to reliably select a new population. After convergence, we extract the optimal parameter set \tilde{w}_{nd} . In our experiments, we use CMA-ES [26] as evolutionary strategy, but the proposed pipeline is extensible to any other genetic algorithm.

Joint adversarial and genetic optimization. For models having differentiable *and* non-differentiable parameters we employ a joint optimization shown in Fig. 4b. We first initialize a set of parameters w , then alternatively use our adversarial strategy (Sec. 3.3.1) for differentiable parameters w_d and the genetic strategy for non differentiable ones w_{nd} . Notice that alternance prevents divergence due to simultaneous optimization. We apply updates until optimum, reaching the two sets of target style parameters, $\tilde{w} = \{\tilde{w}_d, \tilde{w}_{nd}\}$.

3.3.3 Disentanglement guidance

It is worth noting that too sparse injection of model $W_{\text{Mod}}(\cdot)$ negatively impacts disentanglement because the guided-GAN will entangle similar physical traits to fool the discriminator, while injecting too much of $W_{\text{Mod}}(\cdot)$ will prevent the discovery of the disentangled target. Spatially, we observe that regions that do not differ from source to target are most frequently impacted by entanglement. This is because the discriminator naturally provides less reliable predictions due to the local source-target similarities, which leads the generator to produce artifacts resembling target physical characteristics to fool the discriminator, eventually leading to unwanted entanglement. In rainy scenes this happens for trees or buildings, which appearance little vary if dry or wet, whereas ground or road exhibit puddles which are strong rainy cues.

To balance the injection of $W_{\text{Mod}}(\cdot)$, we guide disentanglement by injecting $W_{\text{Mod}}(\cdot)$ only on low domains shift areas, pushing the guided-GAN to learn the disentangled mapping of the scene. Specifically, we learn a Disentanglement Guidance (DG) dataset-wise by averaging the GradCAM [74] feedback on the source dataset, relying on the discriminator D^{ent} gradient on *fake* classification. Areas with high domain shift will be easily identified as *fake*, while others will impact less on the prediction. To take into ac-

count different resolutions, we evaluate GradCAM for all the discriminator layers. Formally, we use LSGAN to obtain

$$\text{DG} = \mathbb{E}_{x \sim P_X(x)} [\mathbb{E}_{l \in L} [\text{GradCAM}_l(D^{\text{ent}}(x))]], \quad (6)$$

with L being the discriminator layers. At training, we inject models only on pixels (u, v) where $\text{DG}_{u,v} < \gamma$, with $\gamma \in [0, 1]$ a hyperparameter. In Sec. 4.4 we visually assess the effect of DG.

4 Experiments

We thoroughly evaluate our guided disentanglement proposal on the real datasets nuScenes [12], RobotCar [63], Cityscapes [17] and WoodScape [91], and on the synthetic Synthia [67] and Weather Cityscapes [24]. The training setup is detailed in Sec. 4.1.1. We extensively test model-guided strategy in Sec. 4.2 on the disentanglement of raindrop, dirt, composite occlusions, and fog – relying on simple physics models. The GAN-guided strategy, requiring rare separate GAN network rendering occlusion traits, is subsequently evaluated in Sec. 4.3 on dirt disentanglement, relying on the recent DirtyGAN [81]. The experiments are all evaluated on a qualitative and quantitative basis, relying on GAN metrics as well as proxy tasks. Our method is compared against the recent DRIT [36], U-GAT-IT [34], AttentionGAN [77], CycleGAN [96], and MUNIT [29] frameworks.

Opposite to the literature, our method enables disentanglement of the target domain, so we report both the disentangled translations as well as the translations with the injection of optimal target occlusions. The disentanglement is greatly visible in still frames of this section, but is also beneficial in video - without any temporal constraints - for our model-guided output (cf. supplementary video). In Sec. 4.2.3, we study the accuracy of our model parameters estimation on the well-documented raindrop model, and ablate our proposal in Sec. 4.4.

4.1 Methodology

Our model-/GAN- guided GAN is architecture agnostic. Here, we rely on MUNIT [29] backbone for its multi-modal capabilities, and exploit LSGAN [52] for training.

For clarity, we formalize trainings as \mathcal{T}_{dis} , where dis is GAN-guided disentanglement ($\mathcal{T}_{W_{\text{GAN}}}$) or model-guided either with differentiable parameters only ($\mathcal{T}_{W_{\text{Mod}}^{w_d}}$) or with full model ($\mathcal{T}_{W_{\text{Mod}}}$). When re-injecting occlusions, we also show their parameters in parentheses. For example, $\mathcal{T}_{W_{\text{Mod}}}(\tilde{w})$ means model-guided disentangled output with re-injection of occlusions with full model estimated on target (\tilde{w}).

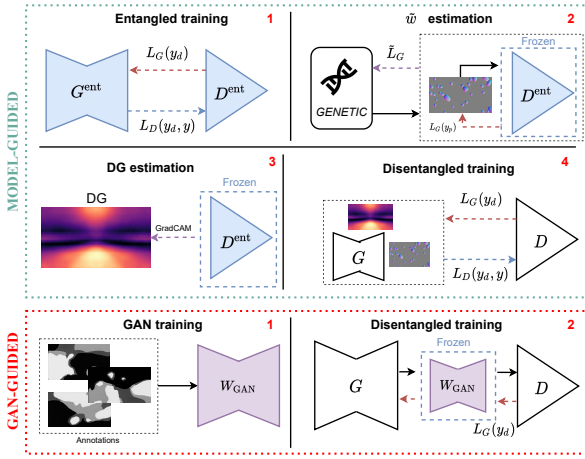


Fig. 5: **Training pipelines.** For *model-guided* disentanglement, we 1) train a naive i2i entangled baseline, 2) use the entangled discriminator feedback to estimate optimal parameters \tilde{w} and 3) Disentanglement Guidance (DG), and finally 4) train the guided-GAN with model injection. For *GAN-guided* disentanglement, we 1) train a GAN (W_{GAN}) exploiting additional knowledge as available semantic annotations and 2) use it to inject target traits during our guided-GAN training.

4.1.1 Training

Fig. 5 shows our two training pipelines.

For **model-guided** training (Fig. 5, top), we leverage on a multi-step pipeline, only assuming the known nature of features to disentangle (e.g. raindrop, dirt, fog, etc.). First, an i2i source \mapsto target baseline is trained in an entangled manner, obtaining entangled discriminator (D^{ent}). Second, we make use of D^{ent} to regress the optimal parameters \tilde{w} with adversarial (Sec. 3.3.1) and genetic (Sec. 3.3.2) estimation. Third, we extract Disentanglement Guidance (Sec. 3.3.3), also using D^{ent} . Finally, we train from scratch the disentangled guided-GAN (Sec. 3.3).

For **GAN-guided** training (Fig. 5, bottom), we use a prior-agnostic two-step pipeline. First, we train W_{GAN} to model elements with adversarial learning, exploiting semantic supervision in our experiments though it could realistically be replaced with self-supervision. Then, we train the disentangled guided-GAN *without* any supervision.

4.1.2 Tasks

Tab. 1 lists the tasks evaluated and ad-hoc datasets. When referring to a task, we denote as indices the entangled features in target domain. Thus, $\text{clear} \mapsto \text{rain}_{\text{drop}}$ means translation from *clear* domain to *rain* domain having entangled *drops*. We later describe models used for disentanglement.

| | Task | Entanglement | Datasets | Guidance |
|-------|--|--------------|----------------------------------|--|
| Model | $\text{clear} \mapsto \text{rain}_{\text{drop}}$ | Raindrop | nuScenes [12] | Model Raindrop $\sigma, t, (s, p) \times 4$ |
| | $\text{gray} \mapsto \text{color}_{\text{dirt}}$ | Dirt | WoodScape [91] | Dirt σ, α |
| | $\text{synth} \mapsto \text{WCS}_{\text{fog}}$ | Fog | Synthia [67], Weather CS [24] | Fog β |
| | $\text{clear} \mapsto \text{snow}_{\text{cmp}}$ | Composite | Synthia [67] | Composite - |
| | $\text{gray} \mapsto \text{color}_{\text{dirt}}$ | Dirt | WoodScape [91] | Network DirtyGAN [81] |

Table 1: **Disentanglement tasks.** For each task, we indicate the features entangled in the target domain (also, shortened as indices of task name), the datasets, and the model or GAN guidance employed for disentanglement.

clear \mapsto rain_{drop} We exploit the recent nuScenes [12] which includes urban driving scenes, and use metadata to build clear/rain splits obtaining 114251/29463 training and 25798/5637 testing clear/rain images. Target rain images entangle highly unfocused drops on the windshield, which would hardly be annotated as seen in Fig. 8, first row.

gray \mapsto color_{dirt} Here, we rely on the recent fish-eye WoodScape [91] dataset which has some images with soiling on the lens. We separate the dataset in clean/dirty images using soiling metadata getting 5117/4873 training images and 500/500 for validation. Because clean/dirty splits do not encompass other domain shifts, we additionally transform *clean* images to *gray*. Subsequently, we frame this as a colorization task where target *color* domain entangles *dirt*. For disentanglement, we experiment using both a physic model-guided and a GAN-guided strategy.

clear \mapsto snow_{cmp} With Synthia [67] we also investigate entanglement of very different alpha-blended composites, like "Confidential" watermarks or fences. We split Synthia using metadata into clear/snow images and further augment snow target with said composite at random position. As clear/fog splits, we use 3634/3739 images for training and 901/947 for validation. To guide disentanglement, we consider a composite model, inspiring from the concept of thin occluders [19].

synth \mapsto WCS_{fog} We learn here the mapping from synthetic Synthia [67] to the foggy version of Weather Cityscapes [24] – a foggy-augmented Cityscapes [17]. The goal is to learn the synthetic to real mapping, while disentangling the complex fog effect in target. For training we use 3634/11900 and 901/2000 for validation as Synthia/WeatherCityscapes. We use a fog model to guide our network.

Note that this task differentiates from others, since target has fog of heterogeneous intensities (max. visibility 750, 375, 150 and 75m) making disentanglement significantly harder.

4.2 Model-guided disentanglement

We first detail the models used for guidance (Sec. 4.2.1) of the model tasks in Tab. 1 and then evaluate the disentanglement performance. Since non-differentiable parameters were fairly easy to manually tune, we thoroughly experiment in the differentiable-only $\{w_d\}$ setup (Sec. 4.2.2), and later compare it to our full $\{w_d, w_{nd}\}$ estimation (Sec. 4.2.3).

4.2.1 Guidance

To correctly fool the discriminator, it is important to choose a model that realistically resembles the entangled feature. We now detail the four models implemented for the model tasks in Tab. 1, detailing differentiable (w_d) and non-differentiable (w_{nd}) parameters. An ablation of the models is done in Sec. 4.4.

Raindrop model. Fig. 6 illustrates our drop occlusion model extending the model of Alletto *et al.* [2], which is balanced between complexity and realism. Drops are approximated by simple trigonometric functions, while we encompass also noise addition for shape variability [1]. For drops photometry, we use fixed displacement maps (U, V) for coordinate mapping on both x and y axes, technically encoded as 3-channels images [2]. To approximate light refraction, a drop at (u, v) has its pixel (u_i, v_i) mapped to

$$(u + U(u_i, v_i) \cdot \rho, v + V(u_i, v_i) \cdot \rho), \quad (7)$$

where ρ is a drop-wise value representing water thickness. Most importantly, we also model imaging focus, since it may extremely impact the rendered raindrop appearance [25, 16, 2]. Hence, we use a Gaussian point spread function [59] to blur synthetic raindrops. We implement kernel variance σ as differentiable, while drops size (s), frequency (p), and shape (t) related parameters are non differentiable. We use a single shape parameter and generate 4 types of drops, with associated p and t .

Dirt model. Here, we naively extend our raindrop model removing displacement maps as soil has no refractive behaviors. Instead, we introduce a color guidance that forces synthetic dirt to be brighter in peripherals regions, also depending on a parameter α which regulates occlusion maximum opacity (hence, maximum α_w value). We also estimate σ as aforementioned. Sample outputs are in Fig. 7.

Composite occlusions model. We exploit the model of thin occluder proposed in [19] to render composite occlusions on images, i.e. randomly translated alpha-blended transparent images such as watermarks or fence-like grids. We assume to fully know transparency, thus no parameter is learned.

Fog model. We leverage the physics model of [24] using an input depth map. Fog thickness is regulated by a differentiable extinction coefficient β which regulates maximum visibility.



Fig. 6: **Raindrop model.** We extend the model of [2] with displacement maps of variable shape and size (left) to model light refraction through, and apply a gaussian blur kernel with σ variance to render out-of-focus appearance (right).



Fig. 7: **Dirt model.** Sample occlusions of our model on WoodScape [91] show the rendered color depends on the soiling transparency. The full degrees of freedom of our dirt model are transparency (α) and defocus blur (σ).

4.2.2 Disentanglement evaluation

In this section, we separate experiments on Raindrop, Dirt and Composite disentanglement from the Fog experiments, since only the former have homogeneous physical parameters (w) throughout the dataset².

Qualitative disentanglement. We present different outputs for the clear \mapsto rain_{drop} trained on nuScenes [12], comparing to state-of-the-art methods [36, 34, 77, 96, 29] (Fig. 8) and for gray \mapsto color_{dirt} and clear \mapsto snow_{cmp} with respect to the backbone (Figs. 9, 10, respectively). In all cases, baselines entangle occlusions in different manners. For instance, in Fig. 8 it is noticeable the constant position of rendered raindrops between different frameworks, as in the 4th column on the leftmost tree, which is a visible effect of entanglement and limits image variability. Also, occlusion entanglement could cause very unrealistic outputs where the structural consistency of either the scene (Fig. 9) or the occlusion (Fig. 10) is completely lost.

Referring to Figs. 8, 9, 10, our method is always able to produce high quality images *without* occlusions (‘disentangled’ row $\mathcal{T}_{W_{\text{Mod}}^{w_d}}$) including typical target domain traits such as wet appearance without drops, colored image without dirt or snowy image without occlusions, respectively. Furthermore, we can inject occlusions with optimal estimated parameters \tilde{w}_d (‘Target-style’ row $\mathcal{T}_{W_{\text{Mod}}^{w_d}}(\tilde{w}_d)$) to mimic target appearance which enables a fair comparison with baselines³.

² For *Raindrop*, *Dirt* and *Composite* we consider w_d and w_{nd} to be dataset-wise constant. E.g. all raindrops have the same defocus blur, transparency, etc. Conversely, *Fog* images have varying fog intensity.

³ For comparing with supervised methods we set $\alpha = 1$ (cf. Sec. 4.3).



Fig. 8: **Raindrop disentanglement on clear \mapsto rain_{drop}**. We compare qualitatively with the state-of-the-art on the clear \mapsto rain_{drop} task with rain drops model-based disentanglement. In the first row, we report samples of the target domain. Subsequently, the *Source* image (2nd row), the translations by different baselines (rows 3-7) and our results (rows 8-11). Our model-guided network is able to disentangle the generation of peculiar rainy characteristics from the drops on the windshield (‘disentangled’ row $\mathcal{T}_{W_{\text{Mod}}}^{w_d}$). In the last rows, we re-inject droplets with the estimated parameters \tilde{w} representing the target style (‘Target-style’ row $\mathcal{T}_{W_{\text{Mod}}}^{w_d}(\tilde{w}_d)$) or other arbitrary styles w_1, w_2 (last 2 rows).

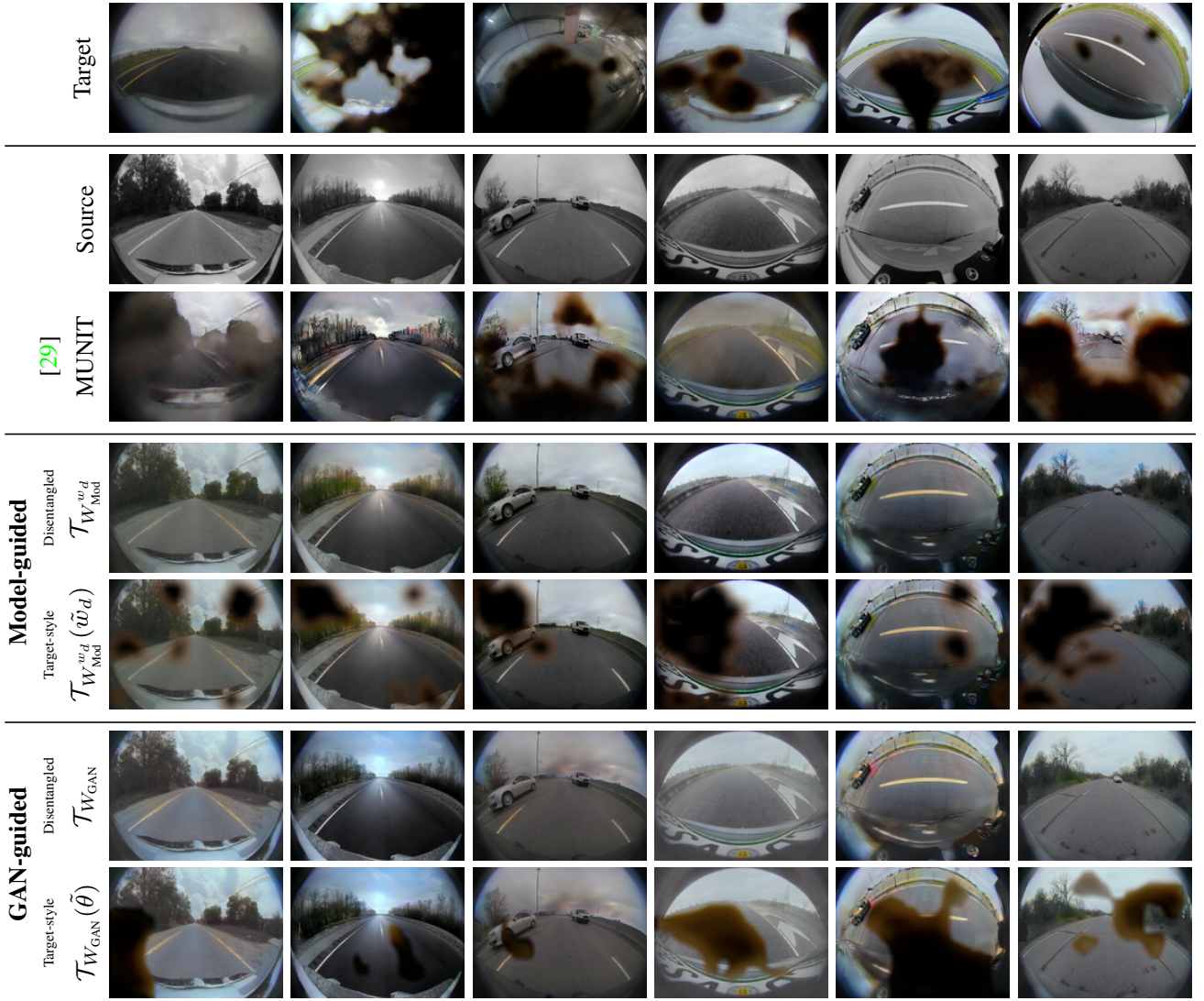


Fig. 9: **Dirt disentanglement on gray \mapsto color_{dirt}**. We compare with MUNIT [29] for the gray \mapsto color_{dirt} task. Although MUNIT successfully mimics the *Target* style (rows 1,3), both model-guided and GAN-guided approaches lead to a more realistic image colorization disentangling the presence of dirt (‘Disentangled’ rows $\mathcal{T}_{W_{\text{Mod}}}$, $\mathcal{T}_{W_{\text{GAN}}}$). Furthermore, we compare dirt generation on the lens with both of our strategies (‘Target-style’ rows $\mathcal{T}_{W_{\text{Mod}}}^{w_d}(\tilde{w}_d)$, $\mathcal{T}_{W_{\text{GAN}}}(\tilde{\theta})$).

We also inject raindrops with arbitrary parameters to simulate *unseen* dashcam-style images in Fig. 8 (last 2 rows). The realistic results demonstrate both the quality of our disentanglement and the realism of the *Raindrop* model.

Quantitative disentanglement. We use GAN metrics to quantify the quality of the learned mappings. Results are reported in Tab. 2a, where Inception Score (IS) [73] evaluates quality and diversity against target, LPIPS distance [94] evaluates translation diversity (thus avoiding mode-collapse), and Conditional Inception Score (CIS) [29] single-image translations diversity for multi-modal baselines. In practice, IS is computed over all the validation set while CIS is estimated on 100 different translations of 100 random images following [29].

The InceptionV3 network for Inception Scores was finetuned on the source/target classification as in [29]. LPIPS distance is calculated on 1900 random pairs of 100 translations as in [29]. For fairness, we only compare our ‘Target-style’ output $\mathcal{T}_{W_{\text{Mod}}}^{w_d}(\tilde{w}_d)$ to baselines, since those are not supposed to disentangle occlusions, and can only output occlusions resembling *Target*.

Tab. 2a shows we outperform all baselines on IS/CIS, including MUNIT – our i2i backbone. This is due to disentanglement, since entanglement phenomena limit occlusions appearance and position variability. Even the scene translation quality is improved by disentanglement since the generator learns a simpler target domain mapping without any occlusions. As regards LPIPS distance, we outperform the baseline

| Experiment | Network | IS \uparrow | LPIPS \uparrow | CIS \uparrow |
|--|--|---------------|------------------|----------------|
| clear \mapsto rain _{drop} | CycleGAN [96] | 1.15 | 0.473 | - |
| | AttentionGAN [77] | 1.41 | 0.464 | - |
| | U-GAT-IT [34] | 1.04 | 0.489 | - |
| | DRIT [36] | 1.19 | 0.492 | 1.12 |
| | MUNIT [29] | 1.21 | 0.495 | 1.03 |
| | Model-guided $\mathcal{T}_{W_{\text{Mod}}^{w_d}}(\tilde{w}_d)$ | 1.53 | 0.515 | 1.15 |
| gray \mapsto color _{dirt} | MUNIT [29] | 1.06 | 0.656 | 1.08 |
| | Model-guided $\mathcal{T}_{W_{\text{Mod}}^{w_d}}(\tilde{w}_d)$ | 1.25 | 0.590 | 1.15 |
| | GAN-guided $\mathcal{T}_{W_{\text{GAN}}}(\tilde{\theta})$ | 1.58 | 0.663 | 1.47 |
| clear \mapsto snow _{cmp} (fence) | MUNIT [29] | 1.26 | 0.547 | 1.11 |
| | Model-guided $\mathcal{T}_{W_{\text{Mod}}^{w_d}}(\tilde{w}_d)$ | 1.31 | 0.539 | 1.19 |
| clear \mapsto snow _{cmp} (WMK) | MUNIT [29] | 1.17 | 0.567 | 1.01 |
| | Model-guided $\mathcal{T}_{W_{\text{Mod}}^{w_d}}(\tilde{w}_d)$ | 1.19 | 0.551 | 1.02 |
| synth \mapsto WCS _{fog} | MUNIT [29] | 1.22 | 0.429 | 1.13 |
| | Model-guided $\mathcal{T}_{W_{\text{Mod}}^{w_d}}(\tilde{w}_d)$ | 1.33 | 0.420 | 1.17 |

(a) GAN metrics.

| Method | AP \uparrow |
|---|---------------|
| Original (from [24]) | 18.7 |
| Finetuned w/ Halder <i>et al.</i> [24] | 25.6 |
| Finetuned w/ Model-guided $\mathcal{T}_{W_{\text{Mod}}^{w_d}}(\tilde{w}_d)$ | 27.7 |

(b) Semantic segmentation

| Network | SSIM \uparrow | PSNR \uparrow |
|--|-----------------|-----------------|
| MUNIT [29] | 0.414 | 13.4 |
| Model-guided $\mathcal{T}_{W_{\text{Mod}}^{w_d}}(\tilde{w}_d)$ | 0.755 | 20.2 |
| GAN-guided $\mathcal{T}_{W_{\text{GAN}}}(\tilde{\theta})$ | 0.724 | 19.3 |

(c) Colorization

Table 2: **Disentanglement evaluation.** In (a), we quantify GAN metrics for all tasks. While quality-aware metrics are always successfully increased, LPIPS depends on the visual complexity of the model and presence of artifacts. In (b), we compare our pipeline for finetuning semantic segmentation network outperforming the state-of-the-art for rain generation. Finally, in (c), we compare our supervised and unsupervised pipeline for unpaired colorization, where both outperform baseline MUNIT [29].

on raindrops while we rank lower on the other tasks. While IS/CIS quantify both quality and diversity, LPIPS metric is evaluating variability only thus penalizing simpler occlusion generation. For instance, our rendered dirt in Fig. 9 is often black while MUNIT-generated artifacts are highly variable (compare rows *MUNIT* and ours $\mathcal{T}_{W_{\text{Mod}}^{w_d}}(\tilde{w}_d)$). The same happens for watermarks in Fig. 10, where unrealistic artifacts are highly variable. For raindrops, instead, MUNIT tends to just blur images, while we benefit from the refractive capabilities of our model which increase LPIPS.

Semantic segmentation. To provide additional insights on the effectiveness of our framework and compensate for the well-known noisiness of GAN metrics [94], we quantify the usability of generated images for semantic segmentation. Therefore, we process the popular Cityscapes [17] dataset for semantic segmentation with our clear \mapsto rain_{drop} model-guided training, obtaining a synthetic rainy version $\mathcal{T}_{W_{\text{Mod}}^{w_d}}(\tilde{w}_d)$ that we use for finetuning PSPNet [95], following Halder *et al.* [24]. Please note that this also demonstrates the generation capabilities to new scenarios of our GAN, since we use the pretrained network on nuScenes given the absence of rainy scenes in Cityscapes. We report the mAP for the 25 rainy images with semantic labels provided by [24] in Tab. 2b. We experience a significant increase (+9%) with respect to baseline PSPNet trained on original clear images (*Original*), and also outperform (+2.1%) the finetuning with rain physics-based rendering [24]. Both networks finetune *Original* weights. The overall low numbers reported are impacted by the significant domain shift between Cityscapes and nuScenes.

Disentanglement on heterogeneous datasets. We now evaluate the effectiveness of the synth \mapsto WCS_{fog} experiment which translates from synthetic Synthia to the real-augmented Weather CityScapes [24] entangling fog of various intensities (from light to thick fog). Notice this task significantly differs from others for two reasons. First, unlike other experiments the model parameter – the optical extinction coefficient, β – varies in the target dataset. Second, the fog model is depending on the scene geometry [55]. This makes the disentanglement task non-trivial. In our adversarial disentanglement, we however still regress a single $\beta = 28.61$ somehow averaging the ground truth values ($\beta \in [4, 40]$).

In Fig. 11 results show we are able to generate images stylistically similar to target ones, but with geometrical consistency and varying β (last 3 rows). Instead, MUNIT [29] fails to preserve realism due to entanglement artifacts, visible in particular on elements at far (as buildings in the background). Please note that we intentionally do not show disentangled output for fairness, since the physical model always blocks the gradient propagation in the sky. More details on this will be discussed in Sec. 5. Randomizing $\beta \in [4, 40]$ we report GAN metrics results in Tab. 2a, where the increased quality of images is quantified. LPIPS distance suffers from the absence of artifacts in our model-guided $\mathcal{T}_{W_{\text{Mod}}^{w_d}}(\tilde{w}_d)$, which artificially increases image variability. The physical model always renders correctly regions at far (e.g. the sky, which is always occluded), hence pure variability quantified by LPIPS is reduced (cf. above LPIPS definition).

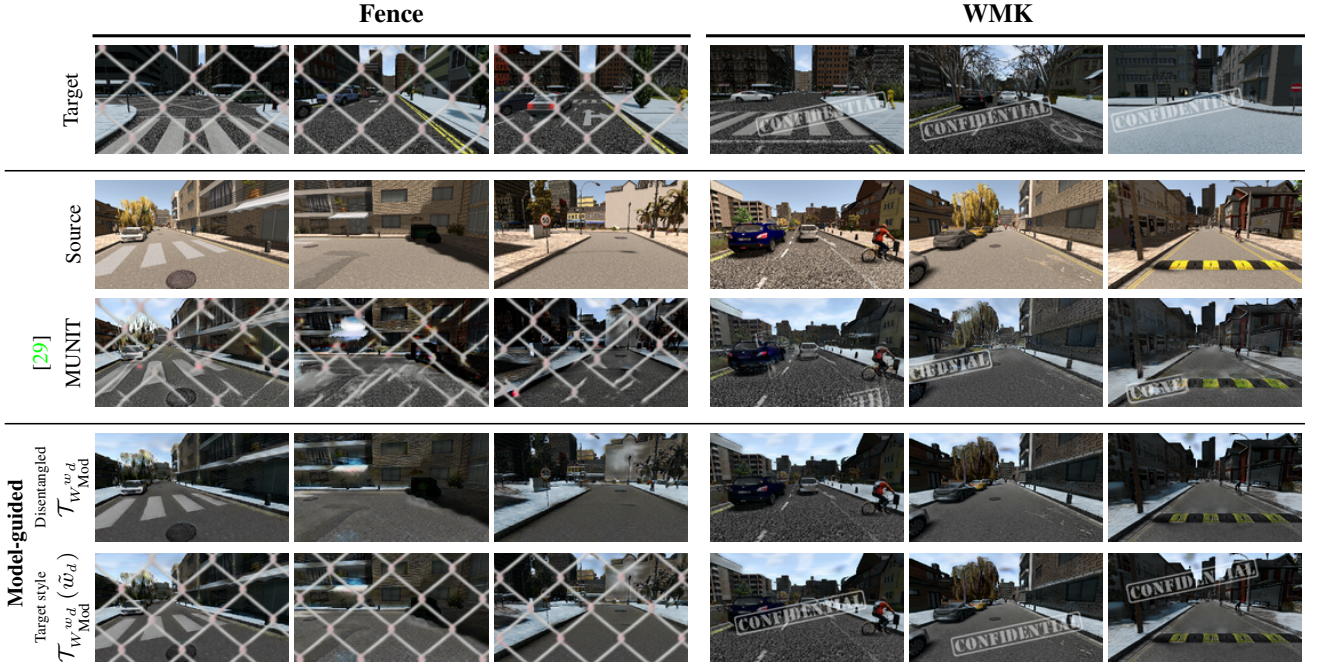


Fig. 10: **Composite disentanglement on clear \mapsto snow_{cmp}**. We extend the applicability of our method to composite occlusions, that we validate in the clear \mapsto snow_{cmp} scenario. We add a fence-like occlusion (left) and a *confidential* watermark (right) to *synthetic_snow*, with random position. As expected, we encounter entanglement phenomena for MUNIT, while our model-guided network is successful in learning the disentangled appearance (‘Disentangled’ row $\mathcal{T}_{W_d^{w_d}}$). In our ‘Target-style’ row $\mathcal{T}_{W_d^{w_d}}(\tilde{w}_d)$, we inject the occlusions to mimic the target style.

4.2.3 Adversarial parameters estimation

We now evaluate the effectiveness of our parameter estimation, considering only differentiable parameters first and later extending to our full system.

Differentiable model ($w = \{w_d\}$). To evaluate realism, we leverage the RobotCar [63] dataset having pairs of clear/raindrop images. Since there is no domain shift between image pairs, we set $G(x) = x$ and regress the defocus blur (σ) again following Sec. 3.3.1. The regressed $\sigma = 3.87$ is used to render raindrops on clear images. Using FID and LPIPS distances we measure perceived distance between real raindrop images and our model-guided raindrops translations ($\mathcal{T}_{W_d^{w_d}}(\tilde{w}_d)$) or the one of Porav et al. [63]. Fig. 12b shows we greatly boost similarity⁴ (-72.02 LPIPS) with real raindrop images. This is qualitatively verified in Fig. 12a, where our rendered raindrops are more similar to *Target*. To provide insights about the quality of our minima, we also evaluate FID for arbitrary σ values ($\sigma \in \{0.0, 2.5, 5.0, 7.5, 10\}$). Fig. 12c proves that our estimated sigma best minimized perceptual distances despite the weak discriminator signal.

⁴ Please note that unlike previous experiments, here LPIPS is used for distance estimation (not diversity), so lower is better.

To measure the accuracy of our differentiable parameter regression (Sec. 3.3.1) we need paired non-occluded/occluded images having occlusions of known physical parameters. To the best of our knowledge such dataset does not exist. Instead, we augment RobotCar [63], WoodScape [91] and Synthia [67] with synthetic raindrops, dirt, and fog, respectively, with gradually increasing values of defocus blur (σ) for raindrop, transparency (α) for dirt⁵ and optical thickness (β) for fog. Using each augmented dataset, we then regress said parameters following Sec. 3.3.1.

Plots in Fig. 13 show estimation versus ground-truth. In average, the estimation error is 0.99% for raindrop, 3.55% for dirt, and 23.51% for fog. The very low σ error for raindrop is to be imputed to the defocus blur that drastically changes scene appearance, while higher error for β must be imputed to the logarithmic dependency of the fog model. Nevertheless, translations preserve realism (cf. Fig. 11).

Full model ($w = \{w_d, w_{nd}\}$). To evaluate the quality of our full raindrop model, we incorporate this time the non-differentiable parameters (i.e. s, p, t) which are estimated with our genetic strategy in Sec. 3.3.2 for 4 types of drops, with a genetic population size of 10. As shown in Fig. 12b,

⁵ In this experiment, we consider dirt with a fixed defocus blur value σ and regress only α to increase the diversity of tasks.

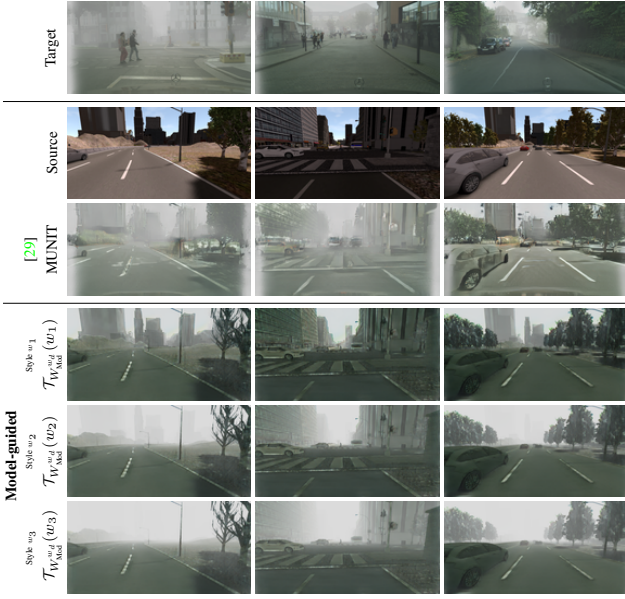


Fig. 11: **synth \mapsto WCS_{fog} translations.** As visible, MUNIT shows entanglement phenomena, leading to artifacts. Our model-guided disentanglement, instead, enables to generate a wide range of foggy images, with arbitrary visibility, while maintaining realism. Since the fog model W_{Mod} always blocks the gradient propagation in the sky region, the network can not achieve photorealistic disentanglement but still improves the generated image quality.

LPIPS metric privileges our full model-guided estimation ($\mathcal{T}_{W_{\text{Mod}}}(\tilde{w})$) while FID suffers compared to using differentiable parameters only. However, we very significantly outperform [63] also qualitatively (Fig. 12a). The mitigated results are explained by the much more complex optimization problem having many more parameters, and by the limited computation time for genetic iterations. However, this let us foresee applications in high-dimensionality problems where manual approximation is not always possible or with a less accurate model (see ablations Sec. 4.4).

Results on the clear \mapsto rain_{drop} task in Fig. 14 are coherent with above insights as the full model estimation, although effective, exhibits slightly lower quality disentanglement.

4.3 GAN-guided disentanglement

Different from model guidance, we now evaluate our method but relying on our GAN-guided strategy for dirt disentanglement in the gray \mapsto color_{dirt} task.

4.3.1 Guidance

For guidance, we exploit DirtyGAN [81], a GAN-based framework for opaque soiling occlusion generation. It is

composed by two components, i.e. a VAE for occlusion map generation (trained using soiling semantic maps) and an i2i network conditioned on the generated map to include synthetic soiling on images. To train DirtyGAN, we first train a VAE to learn the shape of soiling, and then proceed to train a modified CycleGAN [96] to generate realistic soiling, conditioning the soiling shape on the VAE outputs. For more details on this we refer to [81].

4.3.2 Disentanglement evaluation

We leverage here WoodScape [91] datasets having soiling semantic annotation as polygons. Following the GAN-guided pipeline (Fig. 2), DirtyGAN [81] is trained beforehand and frozen during the disentanglement.

Last 2 rows of Fig. 9 show our GAN-guided strategy produces high quality *colored* images *without* occlusions (‘disentangled’ row $\mathcal{T}_{W_{\text{GAN}}}$) while injection of occlusions with optimal estimated parameters $\tilde{\theta}$ (‘Target-style’ row $\mathcal{T}_{W_{\text{GAN}}}(\tilde{\theta})$) also mimics target appearance with an increased variability compared to MUNIT. The use of annotations boosts the overall quality and diversity, which is proved in Tab. 2a where our GAN-guided outperforms both MUNIT baseline and our own model-guided version. Furthermore, since the ground truth for colorization is available, we evaluate in Tab. 2c the effectiveness of disentanglement with SSIM and PSNR metrics (higher is better). While both guided disentanglement outperform MUNIT [29] very significantly, it is noticeable that GAN-guided performs less than model-guided. Arguably, we attribute this to the worse gradient propagation due to more occluded pixels with respect to our physical model⁶.

In the last rows of Fig. 9, we compare visually our model-/GAN-guided disentanglement. Please note that even if the GAN-guided variant captures better variability shape and color of the target occlusions, the model-guided strategy benefit from the defocus blur estimation, ignored in DirtyGAN.

4.4 Ablation studies

We now ablate our proposal. Since GAN-guided cannot be ablated, we focus on the model-guided setting by increasing genetic processing, altering the model complexity, changing the models, or removing disentanglement guidance.

Non-differentiable genetic estimation. We study the effectiveness of our genetic estimation ablating the population size of our raindrop model on RobotCar [63] as in Sec. 4.2.3. We test our algorithm with population size 10/25/50/100,

⁶ On average, DirtyGAN dirt covers 25.4% of the image while our physical model covered 20.1%. While this provides more realistic dirt masks (ground truth annotation is 29.6%) we conjecture this leads to worse gradient propagation.

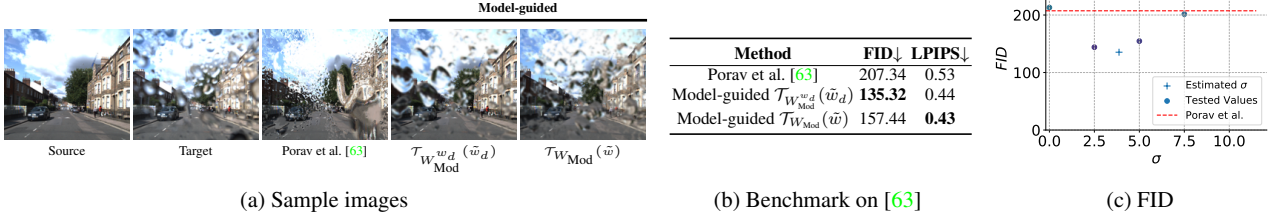


Fig. 12: **Realism of the injected occlusion.** Our defocus blur σ estimation grants an increased realism in raindrop rendering on the RobotCar [63] dataset (a), compared with Porav et al. [63]. This is confirmed by quantitative metrics (b). We report our model-guided translations using either differentiable parameter estimation only ($\mathcal{T}_{W_d^{w_d}}(\tilde{w}_d)$) or the full model estimation ($\mathcal{T}_{W_{Mod}}(\tilde{w})$), outperforming Porav et al. [63] in both. In (c), we evaluate the FID for different σ values in $[0, 10]$, showing that our regressed σ value ($\sigma = 3.81$) actually leads to a local minimum.

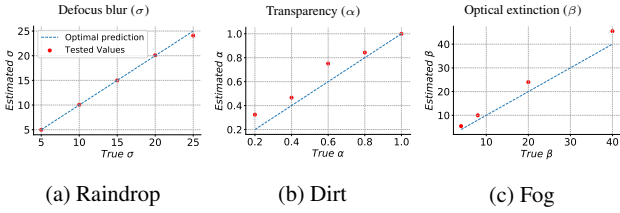


Fig. 13: **Evaluation of the model parameters regression.** The reliability of our parameter estimation is assessed on synthetic datasets augmented with arbitrary physical models acting as ground truth values. Comparing against our regressed value, our strategy performs better when low modifications on the estimated values corresponds to big visual changes (average error is 0.99% for raindrops (a), 3.55% for dirt (b)). For fog (c), we get a higher error of 23.51% due to the low visual impact of high β values.

obtaining FID 157.44/153.32/151.21/**149.09** and LPIPS **0.43**/0.44/0.44/**0.43**. While we observe an obvious increase in performances, this comes with additional computation times, hence we used the lowest population size of 10 for all tests. Nevertheless, this opens doors to potential improvements in the full parametric estimation.

Model complexity. We study the influence of the model on disentanglement for the clear \mapsto rain_{drop} on nuScenes [12] task. Specifically, we evaluate three raindrop models of decreasing complexity: 1) Our model from Sec. 4.2.1 (named *Ours*). 2) The same model but without shape and thickness variability (*Refract*), and 3) A naive non-parametric colored Gaussian-shape model (*Gaussian*). Note that *Gaussian* is deprived of any refractive property as it uses fixed color, and does not regress any physical parameters.

In Fig. 15a, we report GAN metrics for all models translations following Sec. 4.2. Even if increasing complexity of the model is beneficial for disentanglement, very simple models still lead to a performance boost. We advocate the best per-

formances of *Ours* to a more effective discriminator fooling during training, as a consequence of increased realism.

Model choice. To also evaluate whether injected features only behave as adversarial noise regardless of the chosen model, we trained on RobotCar [63] (as in Sec. 4.2.3) though purposely using an incorrect model as watermark, dirt, fence. Evaluating the FID against real raindrop images, we measure **135.32** (raindrop) / 329.17 (watermark) / 334.76 (dirt) / 948.71 (fence), proving necessity of using the ad-hoc model.

Disentanglement Guidance (DG). We use the nuScenes clear \mapsto rain_{drop} task to visualize the effects of different DG strategies (Sec. 3.3.3). For varying values of the DG threshold γ in Fig. 15b we see results ranging from no guidance ($\gamma = 0$) to strict guidance ($\gamma = 1$). With lax guidance ($\gamma = 0$), we fall back in the baseline scenario with visible entanglement effects, while with $\gamma = 1$ we do achieve disentanglement, at the cost of losing important visual features as reflections on the road. Only appropriate guidance ($\gamma = 0.75$) achieves disentanglement and preserves realism.

5 Discussion

To our best knowledge, we have designed the first unsupervised strategy to disentangle physics-based features in i2i. The good qualitative and quantitative performance showcase promising interest for several applications, still they are peculiar points and limitations which we now discuss.

Independence assumption. For unsupervised disentanglement, we assume the physical model to be completely independent from the scene, in order to use our intuition about marginal separation (see Sec. 3.1 and Eq. 2). However, since physical models may need the underlying scene to correctly render desired traits, one may argue their appearance is not completely disentangled. While this is true from a visual

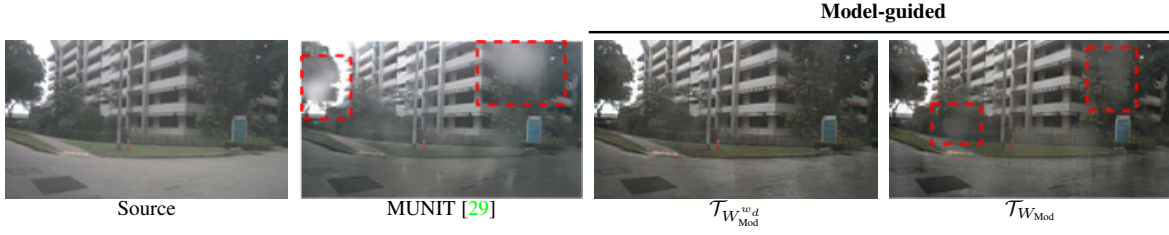


Fig. 14: **Full model estimation on clear \mapsto rain_{drop}**. With complete parameter estimation ($\mathcal{T}_{W_{\text{Mod}}}$, rightmost), we achieve a slightly worse disentanglement than with manually-tuned non-differentiable parameters ($\mathcal{T}_{W_{\text{Mod}}}^{w_d}$), visible in red areas of $\mathcal{T}_{W_{\text{Mod}}}$. However, in both of our translations we generate typical rain traits as reflections with reasonable disentanglement, while baseline MUNIT [29] has very evident raindrops entangled highlighted in red.

| Model | IS \uparrow | LPIPS \uparrow | CIS \uparrow |
|----------|---------------|------------------|----------------|
| none | 1.21 | 0.50 | 1.03 |
| Gaussian | 1.35 | 0.51 | 1.13 |
| Refract | 1.46 | 0.50 | 1.12 |
| Ours | 1.53 | 0.52 | 1.15 |

(a) Model complexity

(b) Disentanglement Guidance

Fig. 15: **Ablations of model complexity and Disentanglement Guidance**. In (a), we quantify disentanglement effects with simpler model having less variability (*Refract*), or only color guidance (*Gaussian*). Even if complexity is beneficial for disentanglement (*Ours*), simple models permits disentanglement to some extent. In (b), we study the efficacy of the Disentanglement Guidance (DG) for different γ values on clear \mapsto rain_{drop} task. With $\gamma = 0$ our approach fallbacks to the baseline and entangles occlusions, while with guidance $\gamma = 1$ the translation lacks important features such as reflections and glares. With $\gamma = 0.75$ we simultaneously avoid entanglements and preserve translation capabilities.

point of view, it is not from a physical one. Let's interpret disentanglement properties to be dependent on scene *elements*. In presence of disentanglement, the same physical model could be applied to different objects regardless of what they are. For instance, we could use the same raindrop refraction map on either roads or buildings with identical parameters. In this sense, $G(x)$ dependency in physical models is not impacting our visual independence assumption.

On partial entanglement issues. We observe in some cases that gradient propagation can be affected by fixed entanglement of occlusion features. This is the case for example for sky regions in fog (Sec. 4.2.2) because physics [55] formalizes that regardless of its intensity fog is always entangled at far. In such scenarios, disentanglement will perform poorly because the generator will not get any discriminative feedback. In many other cases however, Disentanglement Guidance (DG, Sec. 3.3.3) mitigates the phenomenon as it blocks injection of the physical model in relevant image regions. We conjecture that the effectiveness could be extended by varying DG at training time to ensure a balanced gradient propagation.

On genetic estimation effectiveness. The sub-optimal performances of our genetic estimation of w_{nd} are imputed to the much more complex search space, in which we vary all

parameters of our physical model simultaneously. Although we did set fairly large search limits for w_{nd} , one could envisage a mixed training in which the search space is limited to reasonable hand-tuned limits. In this sense, genetic estimation of w_{nd} could be seen as a minimum mining technique, ensuring increased performances on the hand-tuned values.

References

1. Rain drops on screen. <https://www.shadertoy.com/view/ldSBWW> 8
2. Alletto, S., Carlin, C., Rigazio, L., Ishii, Y., Tsukizawa, S.: Adherent raindrop removal with self-supervised attention maps and spatio-temporal generative adversarial networks. In: ICCV Workshops (2019) 2, 3, 8
3. Amodio, M., Krishnaswamy, S.: Travelgan: Image-to-image translation by transformation vector learning. In: CVPR (2019) 2
4. Anokhin, I., Solovlev, P., Korzhnikov, D., Kharlamov, A., Khakhulin, T., Silvestrov, A., Nikolenko, S., Lempitsky, V., Sterkin, G.: High-resolution daytime translation without domain labels. In: CVPR (2020) 2
5. Anoosheh, A., Agustsson, E., Timofte, R., Van Gool, L.: Combogan: Unrestrained scalability for image domain translation. In: CVPR Workshops (2018) 2
6. Arar, M., Ginger, Y., Danon, D., Bermano, A.H., Cohen-Or, D.: Unsupervised multi-modal image registration via geometry preserving image-to-image translation. In: CVPR (2020) 2
7. Barnum, P.C., Narasimhan, S., Kanade, T.: Analysis of rain and snow in frequency space. IJCV (2010) 3
8. Benaim, S., Wolf, L.: One-sided unsupervised domain mapping. In: NeurIPS (2017) 2

9. Bepler, T., Zhong, E., Kelley, K., Brignole, E., Berger, B.: Explicitly disentangling image content from translation and rotation with spatial-vae. In: *NeurIPS* (2019) [2](#)
10. Bhattacharjee, D., Kim, S., Vizier, G., Salzmann, M.: Dunit: Detection-based unsupervised image-to-image translation. In: *CVPR* (2020) [2](#)
11. Bi, S., Sunkavalli, K., Perazzi, F., Shechtman, E., Kim, V.G., Ramamoorthi, R.: Deep cg2real: Synthetic-to-real translation via image disentanglement. In: *ICCV* (2019) [1](#), [2](#)
12. Caesar, H., Bankiti, V., Lang, A.H., Vora, S., Liong, V.E., Xu, Q., Krishnan, A., Pan, Y., Baldan, G., Beijbom, O.: nuscenes: A multimodal dataset for autonomous driving. In: *CVPR* (2020) [6](#), [7](#), [8](#), [14](#)
13. Cherian, A., Sullivan, A.: Sem-gan: Semantically-consistent image-to-image translation. In: *WACV* (2019) [2](#)
14. Choi, Y., Choi, M., Kim, M., Ha, J.W., Kim, S., Choo, J.: Stargan: Unified generative adversarial networks for multi-domain image-to-image translation. In: *CVPR* (2018) [2](#)
15. Choi, Y., Uh, Y., Yoo, J., Ha, J.W.: Stargan v2: Diverse image synthesis for multiple domains. In: *CVPR* (2020) [2](#)
16. Cord, A., Aubert, D.: Towards rain detection through use of in-vehicle multipurpose cameras. In: *IV* (2011) [8](#)
17. Cordts, M., Omran, M., Ramos, S., Rehfeld, T., Enzweiler, M., Benenson, R., Franke, U., Roth, S., Schiele, B.: The cityscapes dataset for semantic urban scene understanding. In: *CVPR* (2016) [6](#), [7](#), [11](#)
18. Fu, H., Gong, M., Wang, C., Batmanghelich, K., Zhang, K., Tao, D.: Geometry-consistent generative adversarial networks for one-sided unsupervised domain mapping. In: *CVPR* (2019) [2](#)
19. Garg, K., Nayar, S.K.: Photorealistic rendering of rain streaks. *ACM TOG* (2006) [3](#), [7](#), [8](#)
20. Gomez, R., Liu, Y., De Nadai, M., Karatzas, D., Lepri, B., Sebe, N.: Retrieval guided unsupervised multi-domain image to image translation. In: *MM* (2020) [2](#)
21. Gong, R., Dai, D., Chen, Y., Li, W., Van Gool, L.: Analogical image translation for fog generation. In: *AAAI* (2021) [2](#)
22. Gong, R., Li, W., Chen, Y., Gool, L.V.: Dlow: Domain flow for adaptation and generalization. In: *CVPR* (2019) [2](#)
23. Gu, J., Ramamoorthi, R., Belhumeur, P., Nayar, S.: Removing image artifacts due to dirty camera lenses and thin occluders. In: *SIGGRAPH* (2009) [3](#)
24. Halder, S.S., Lalonde, J.F., de Charette, R.: Physics-based rendering for improving robustness to rain. In: *ICCV* (2019) [2](#), [3](#), [4](#), [6](#), [7](#), [8](#), [11](#)
25. Halimeh, J.C., Roser, M.: Raindrop detection on car windshields using geometric-photometric environment construction and intensity-based correlation. In: *IV* (2009) [8](#)
26. Hansen, N., Müller, S.D., Koumoutsakos, P.: Reducing the time complexity of the derandomized evolution strategy with covariance matrix adaptation (cma-es). *Evolutionary computation* (2003) [5](#), [6](#)
27. Hao, Z., You, S., Li, Y., Li, K., Lu, F.: Learning from synthetic photorealistic raindrop for single image raindrop removal. In: *ICCV Workshops* (2019) [3](#)
28. Hoffman, J., Tzeng, E., Park, T., Zhu, J.Y., Isola, P., Saenko, K., A., E.A., Darrell, T.: CyCADA: Cycle consistent adversarial domain adaptation. In: *ICML* (2018) [1](#)
29. Huang, X., Liu, M.Y., Belongie, S., Kautz, J.: Multimodal unsupervised image-to-image translation. In: *ECCV* (2018) [2](#), [5](#), [6](#), [8](#), [9](#), [10](#), [11](#), [12](#), [13](#), [15](#)
30. Hui, L., Li, X., Chen, J., He, H., Yang, J.: Unsupervised multi-domain image translation with domain-specific encoders/decoders. In: *ICPR* (2018) [2](#)
31. Isola, P., Zhu, J.Y., Zhou, T., Efros, A.A.: Image-to-image translation with conditional adversarial networks. In: *CVPR* (2017) [1](#), [2](#)
32. Jia, Z., Yuan, B., Wang, K., Wu, H., Clifford, D., Yuan, Z., Su, H.: Lipschitz regularized cyclegan for improving semantic robustness in unpaired image-to-image translation. *arXiv* (2020) [2](#)
33. Jiang, L., Zhang, C., Huang, M., Liu, C., Shi, J., Loy, C.C.: Tsit: A simple and versatile framework for image-to-image translation. In: *ECCV* (2020) [2](#)
34. Kim, J., Kim, M., Kang, H., Lee, K.: U-gat-it: unsupervised generative attentional networks with adaptive layer-instance normalization for image-to-image translation. In: *ICLR* (2020) [2](#), [6](#), [8](#), [9](#), [11](#)
35. Kondo, R., Kawano, K., Koide, S., Kutsuna, T.: Flow-based image-to-image translation with feature disentanglement. In: *NeurIPS* (2019) [2](#)
36. Lee, H.Y., Tseng, H.Y., Mao, Q., Huang, J.B., Lu, Y.D., Singh, M., Yang, M.H.: Drit++: Diverse image-to-image translation via disentangled representations. *IJCV* (2020) [2](#), [6](#), [8](#), [9](#), [11](#)
37. Li, P., Liang, X., Jia, D., Xing, E.P.: Semantic-aware grad-gan for virtual-to-real urban scene adaption. *BMVC* (2018) [2](#)
38. Li, X., Zhang, S., Hu, J., Cao, L., Hong, X., Mao, X., Huang, F., Wu, Y., Ji, R.: Image-to-image translation via hierarchical style disentanglement. In: *CVPR* (2021) [2](#)
39. Li, Y., Yuan, L., Vasconcelos, N.: Bidirectional learning for domain adaptation of semantic segmentation. In: *CVPR* (2019) [1](#)
40. Lin, C.T., Wu, Y.Y., Hsu, P.H., Lai, S.H.: Multimodal structure-consistent image-to-image translation. In: *AAAI* (2020) [2](#)
41. Lin, J., Chen, Z., Xia, Y., Liu, S., Qin, T., Luo, J.: Exploring explicit domain supervision for latent space disentanglement in unpaired image-to-image translation. *T-PAMI* (2019) [2](#)
42. Lin, Y., Wang, Y., Li, Y., Gao, Y., Wang, Z., Khan, L.: Attention-based spatial guidance for image-to-image translation. In: *WACV* (2021) [2](#)
43. Lin, Y., Wang, Y., Li, Y., Gao, Y., Wang, Z., Khan, L.: Attention-based spatial guidance for image-to-image translation. In: *WACV* (2021) [2](#)
44. Lira, W., Merz, J., Ritchie, D., Cohen-Or, D., Zhang, H.: Ganhopper: Multi-hop gan for unsupervised image-to-image translation. In: *ECCV* (2020) [2](#)
45. Liu, M.Y., Breuel, T., Kautz, J.: Unsupervised image-to-image translation networks. In: *NeurIPS* (2017) [1](#), [2](#)
46. Liu, M.Y., Huang, X., Mallya, A., Karras, T., Aila, T., Lehtinen, J., Kautz, J.: Few-shot unsupervised image-to-image translation. In: *ICCV* (2019) [2](#)
47. Liu, Y., Li, Y., You, S., Lu, F.: Unsupervised learning for intrinsic image decomposition from a single image. In: *CVPR* (2020) [2](#)
48. Liu, Y., Sangineto, E., Chen, Y., Bao, L., Zhang, H., Sebe, N., Lepri, B., Wang, W., De Nadai, M.: Smoothing the disentangled latent style space for unsupervised image-to-image translation. In: *CVPR* (2021) [2](#)
49. Lütjens, B., Leshchinskiy, B., Requena-Mesa, C., Chishtie, F., Díaz-Rodríguez, N., Boulais, O., Piña, A., Newman, D., Lavin, A., Gal, Y., Raïssi, C.: Physics-informed gans for coastal flood visualization. *arXiv* (2020) [2](#)
50. Ma, L., Jia, X., Georgoulis, S., Tuytelaars, T., Van Gool, L.: Exemplar guided unsupervised image-to-image translation with semantic consistency. In: *ICLR* (2019) [2](#)
51. Ma, S., Fu, J., Wen Chen, C., Mei, T.: Da-gan: Instance-level image translation by deep attention generative adversarial networks. In: *CVPR* (2018) [2](#)
52. Mao, X., Li, Q., Xie, H., Lau, R.Y., Wang, Z., Paul Smolley, S.: Least squares generative adversarial networks. In: *ICCV* (2017) [3](#), [6](#)
53. Mejjati, Y.A., Richardt, C., Tompkin, J., Cosker, D., Kim, K.I.: Unsupervised attention-guided image-to-image translation. In: *NeurIPS* (2018) [2](#)
54. Mo, S., Cho, M., Shin, J.: Instagan: Instance-aware image-to-image translation. *ICLR* (2019) [2](#)
55. Narasimhan, S.G., Nayar, S.K.: Vision and the atmosphere. *IJCV* (2002) [11](#), [15](#)
56. Nguyen, T.P., Lathuilière, S., Ricci, E.: Multi-domain image-to-image translation with adaptive inference graph. In: *ICPR* (2021) [2](#)

57. Nizan, O., Tal, A.: Breaking the cycle-colleagues are all you need. In: CVPR (2020) [2](#)
58. Park, T., Efros, A.A., Zhang, R., Zhu, J.Y.: Contrastive learning for unpaired image-to-image translation. In: ECCV (2020) [2](#)
59. Pentland, A.P.: A new sense for depth of field. T-PAMI (1987) [8](#)
60. Pizzati, F., Cerri, P., de Charette, R.: Model-based occlusion disentanglement for image-to-image translation. ECCV (2020) [2](#)
61. Pizzati, F., Cerri, P., de Charette, R.: CoMoGAN: continuous model-guided image-to-image translation. In: CVPR (2021) [2](#)
62. Pizzati, F., de Charette, R., Zaccaria, M., Cerri, P.: Domain bridge for unpaired image-to-image translation and unsupervised domain adaptation. In: WACV (2020) [1](#), [3](#)
63. Porav, H., Bruls, T., Newman, P.: I can see clearly now: Image restoration via de-raining. In: ICRA (2019) [3](#), [6](#), [12](#), [13](#), [14](#)
64. Qu, Y., Chen, Y., Huang, J., Xie, Y.: Enhanced pix2pix dehazing network. In: CVPR (2019) [1](#)
65. Ramirez, P.Z., Tonioni, A., Di Stefano, L.: Exploiting semantics in adversarial training for image-level domain adaptation. In: IPAS (2018) [2](#)
66. Romero, A., Arbeláez, P., Van Gool, L., Timofte, R.: Smit: Stochastic multi-label image-to-image translation. In: ICCV Workshops (2019) [2](#)
67. Ros, G., Sellart, L., Materzynska, J., Vazquez, D., Lopez, A.M.: The synthia dataset: A large collection of synthetic images for semantic segmentation of urban scenes. In: CVPR (2016) [6](#), [7](#), [12](#)
68. Roser, M., Geiger, A.: Video-based raindrop detection for improved image registration. In: ICCV Workshops (2009) [2](#), [3](#)
69. Roser, M., Kurz, J., Geiger, A.: Realistic modeling of water droplets for monocular adherent raindrop recognition using bezier curves. In: ACCV (2010) [3](#)
70. Rousseau, P., Jolivet, V., Ghazanfarpour, D.: Realistic real-time rain rendering. Computers & Graphics (2006) [3](#)
71. Saito, K., Saenko, K., Liu, M.Y.: Coco-funit: Few-shot unsupervised image translation with a content conditioned style encoder. In: ECCV (2020) [2](#)
72. Sakaridis, C., Dai, D., Van Gool, L.: Semantic foggy scene understanding with synthetic data. IJCV (2018) [3](#), [4](#)
73. Salimans, T., Goodfellow, I., Zaremba, W., Cheung, V., Radford, A., Chen, X.: Improved techniques for training gans. In: NeurIPS (2016) [10](#)
74. Selvaraju, R.R., Cogswell, M., Das, A., Vedantam, R., Parikh, D., Batra, D.: Grad-cam: Visual explanations from deep networks via gradient-based localization. In: ICCV (2017) [6](#)
75. Shen, Z., Huang, M., Shi, J., Xue, X., Huang, T.S.: Towards instance-level image-to-image translation. In: CVPR (2019) [1](#), [2](#)
76. Singh, K.K., Ojha, U., Lee, Y.J.: Finegan: Unsupervised hierarchical disentanglement for fine-grained object generation and discovery. In: CVPR (2019) [2](#)
77. Tang, H., Xu, D., Sebe, N., Yan, Y.: Attention-guided generative adversarial networks for unsupervised image-to-image translation. In: International Joint Conference on Neural Networks (IJCNN) (2019) [2](#), [6](#), [8](#), [9](#), [11](#)
78. Tang, H., Xu, D., Yan, Y., Corso, J.J., Torr, P.H., Sebe, N.: Multi-channel attention selection gans for guided image-to-image translation. In: CVPR (2019) [2](#)
79. Toldo, M., Maracani, A., Michieli, U., Zanuttigh, P.: Unsupervised domain adaptation in semantic segmentation: a review. Technologies (2020) [1](#)
80. Tremblay, M., Halder, S.S., de Charette, R., Lalonde, J.F.: Rain rendering for evaluating and improving robustness to bad weather. IJCV (2020) [2](#), [3](#)
81. Uricar, M., Sistu, G., Rashed, H., Vobecky, A., Krizek, P., Burger, F., Yogamani, S.: Let's get dirty: Gan based data augmentation for soiling and adverse weather classification in autonomous driving. In: WACV (2021) [6](#), [7](#), [13](#)
82. Wang, T.C., Liu, M.Y., Zhu, J.Y., Tao, A., Kautz, J., Catanzaro, B.: High-resolution image synthesis and semantic manipulation with conditional gans. In: CVPR (2018) [2](#)
83. Weber, Y., Jolivet, V., Gilet, G., Ghazanfarpour, D.: A multiscale model for rain rendering in real-time. Computers & Graphics (2015) [3](#)
84. Wu, P.W., Lin, Y.J., Chang, C.H., Chang, E.Y., Liao, S.W.: Relgan: Multi-domain image-to-image translation via relative attributes. In: ICCV (2019) [2](#)
85. Wu, W., Cao, K., Li, C., Qian, C., Loy, C.C.: Transgaga: Geometry-aware unsupervised image-to-image translation. In: CVPR (2019) [2](#)
86. Xia, W., Yang, Y., Xue, J.H.: Unsupervised multi-domain multi-modal image-to-image translation with explicit domain-constrained disentanglement. Neural Networks (2020) [2](#)
87. Xie, Y., Franz, E., Chu, M., Thuerey, N.: tempoGAN: A temporally coherent, volumetric gan for super-resolution fluid flow. SIGGRAPH (2018) [1](#)
88. Yang, X., Xie, D., Wang, X.: Crossing-domain generative adversarial networks for unsupervised multi-domain image-to-image translation. In: MM (2018) [2](#)
89. Yang, X., Xu, Z., Luo, J.: Towards perceptual image dehazing by physics-based disentanglement and adversarial training. In: AAAI (2018) [2](#)
90. Yi, Z., Zhang, H., Tan, P., Gong, M.: Dualgan: Unsupervised dual learning for image-to-image translation. In: ICCV (2017) [2](#)
91. Yogamani, S., Hughes, C., Horgan, J., Sistu, G., Varley, P., O'Dea, D., Uricar, M., Milz, S., Simon, M., Amende, K., et al.: Woodscape: A multi-task, multi-camera fisheye dataset for autonomous driving. In: ICCV (2019) [6](#), [7](#), [8](#), [12](#), [13](#)
92. You, S., Tan, R.T., Kawakami, R., Mukaigawa, Y., Ikeuchi, K.: Adherent raindrop modeling, detection and removal in video. T-PAMI (2015) [3](#)
93. Yu, X., Chen, Y., Liu, S., Li, T., Li, G.: Multi-mapping image-to-image translation via learning disentanglement. In: Advances in Neural Information Processing Systems (2019) [2](#)
94. Zhang, R., Isola, P., Efros, A.A., Shechtman, E., Wang, O.: The unreasonable effectiveness of deep features as a perceptual metric. In: CVPR (2018) [10](#), [11](#)
95. Zhao, H., Shi, J., Qi, X., Wang, X., Jia, J.: Pyramid scene parsing network. In: CVPR (2017) [11](#)
96. Zhu, J.Y., Park, T., Isola, P., Efros, A.A.: Unpaired image-to-image translation using cycle-consistent adversarial networks. In: CVPR (2017) [1](#), [2](#), [6](#), [8](#), [9](#), [11](#), [13](#)
97. Zhu, J.Y., Zhang, R., Pathak, D., Darrell, T., Efros, A.A., Wang, O., Shechtman, E.: Toward multimodal image-to-image translation. In: NeurIPS (2017) [2](#)
98. Zhu, P., Abdal, R., Qin, Y., Wonka, P.: Sean: Image synthesis with semantic region-adaptive normalization. In: CVPR (2020) [2](#)
99. Zhu, Z., Xu, Z., You, A., Bai, X.: Semantically multi-modal image synthesis. In: CVPR (2020) [2](#)